Integrative Biology

PAPER

View Article Online
View Journal | View Issue



Cite this: *Integr. Biol.*, 2014, 6, 184

# Bacterial nucleoid structure probed by active drag and resistive pulse sensing

Vivek V. Thacker,†[a] Krystyna Bromek,†[a] Benoit Meijer,[a] Jurij Kotar,[a] Bianca Sclavi,[b] Marco Cosentino Lagomarsino,[c] Ulrich F. Keyser[a] and Pietro Cicuta*[a]

Received 14th July 2013,
Accepted 21st November 2013

DOI: 10.1039/c3ib40147b

www.rsc.org/ibiology

Recent biophysical approaches have provided key insights into the enthalpic and entropic forces that compact the nucleoid in the cell. Our biophysical approach combines two complementary, non-invasive and label-free techniques: a precisely timed steerable optical trap and a high throughput microcapillary Coulter counter. We demonstrate the ability of the latter technique to probe the physical properties and size of many purified nucleoids, at the individual nucleoid level. The DNA-binding protein H-NS is central to the organization of the bacterial genome. Our results show that nucleoids purified from the Δhns strain in the stationary phase expand approximately five fold more than the form observed in WT bacteria. This compaction is consistent with the role played by H-NS in regulating the nucleoid structure and the significant organizational changes that occur as the cell adapts to the stationary phase. We also study the permeability to the flow of ions and find that in the experiment nucleoids behave as solid colloids.

**Insight, innovation, integration**

The role of Nucleoid Associated Proteins (NAPs) in structuring the bacterial nucleoid has been previously studied using biophysical methods, but most of these are unsuited for high-throughput lab-on-chip approaches. Our novel experimental approach is to use steerable optical traps to measure the drag coefficient of nucleoids, and hence their size, thus calibrating the high throughput signals from a custom microcapillary Coulter counter setup. These complementary techniques enable us to study changes in global nucleoid organisation of entire populations but resolving at the single nucleoid level. The power of this method is demonstrated by showing the increase in nucleoid size as a result of deletion of the NAP H-NS, on *E. coli* bacteria entering the stationary phase – a result consistent with the biological role of H-NS. The microcapillary experiments also reveal that nucleoids behave as solid colloids and are impermeable to ionic flow, a new insight into nucleoid organisation.

## 1 Introduction

Within the cell, bacterial DNA exists as a nucleoprotein complex known as the nucleoid, which occupies a small, well-defined cytoplasmic volume despite the lack of a surrounding membrane.[1,2] This compaction is believed to occur due to a combination of osmotic and enthalpic effects.[3–7] The structural organization of the nucleoid is thought to play a role in the transcription regulation that mediates the celluar response to changing environmental cues.[8] The important role of Nucleoid Associated Proteins (NAPs) in maintaining this organization[9,10] can be gauged from the fact that when the cells are lysed and nucleoids released, the NAPs dissociate from the nucleoid very slowly[4] and the nucleoids retain part of their compactness[11–13] over a timescale of tens of minutes.

The DNA-binding H-NS (Histone-like Nucleoid Structuring) protein is one of the most important NAPs known to affect nucleoid organization.[14,15] Individual proteins bind at different points along the chromosome and then form dimers, resulting in H-NS–DNA bridges. *In vitro* analyses show the formation of a rigid nucleoprotein filament, which could act as a zipper to stabilize supercoiled DNA[14,16–18] or silence gene expression.[19,20] Although the deletion of the *hns* gene has only a small effect on the growth rate,[21,22] it can result in extensive chromosome restructuring.[23] On the other hand, when WT (wild type *E. coli*) cells enter the stationary growth phase due to a depletion of nutrients, global changes in the set of NAPs bound on the nucleoid lead to changes in its compaction and supercoiling organization.[9] The combination of these two effects could result in substantial differences in the size and compactness of nucleoids from the WT and Δhns (mutant lacking the *hns* gene) strains especially as these cells progress into the stationary phase.

[a] *Cavendish Laboratory, University of Cambridge, JJ Thompson Avenue, Cambridge CB3 0HE, UK. E-mail: pc245@cam.ac.uk*
[b] *CNRS/Ecole Normale Supérieure de Cachan, Cachan, France*
[c] *Genomic Physics Group, FRE 3214 CNRS, Paris, France*
† These authors contributed equally to this work.

A direct way to study this is to quantify the size of the nucleoids soon after release from the cell, when they retain their compactness, ideally using a high-throughput biophysical technique.

The role of NAPs in structuring the nucleoid has been studied in recent years using *in vitro* biophysical methods,[24–26] *in vivo* imaging studies[23] and most recently with a combination of fluorescence, confinement and force measurements using optical tweezers.[4] However, most of these methods are unsuited for high-throughput lab-on-chip approaches. In these studies the overall size of the nucleoid has been determined by measuring the ellipsoid surrounding a defined fraction (typically 50%) of the fluorescence intensity of stained DNA.[27,28] The intercalating dyes used in these staining protocols can affect the physical and structural properties of the DNA helix[28] and do not provide an unambiguous handle for the size of the nucleoid (see Fig. 1a).

To address these issues, we demonstrate two complementary and label-free methods sensitive to the size of nucleoids in solution: measurements of drag by optical tweezers, which are easily calibrated but limited to small numbers of nucleoids, and resistive pulse sensing which is a high-throughput method ($\sim$30 nucleoids min$^{-1}$) (Fig. 1b and c). The resistive pulse sensing is applied here for the first time to nucleoids using pressure driven flows in microcapillaries. We validate these methods on a biophysical question of current interest, and study the effects that both the deletion of the *hns* gene and the cellular adaptation to different stages of bacterial growth (Fig. 1a) have on the compaction of the entire *E. coli* nucleoid. By direct comparison with solid polystyrene colloids, we also show that nucleoids are relatively impermeable to the flow of ions.

## 2 Results

### 2.1 Overview of microcapillary experiments

A schematic of the microcapillary experimental setup is shown in Fig. 1b. The resistive pulse technique measures the ionic current through a pore in an insulating membrane that connects two reservoirs filled with an electrolyte. The particles to be probed translocate through the pore under the influence of either pressure or electrophoretic attraction. As they pass through the pore, they temporarily reduce the flux of ions and can be detected by characteristic changes in the ionic current.[29–31] We have recently demonstrated the fabrication of pores from glass capillaries, effective at both the micro and nanoscale.[32–34] The microcapillary is sealed into a custom-designed *Polydimethylsiloxane* (PDMS) mold and connects two reservoirs filled with the 1 mM NaCl nucleoid extraction buffer (see the Methods section). A solution of nucleoids in the same buffer is then introduced into the

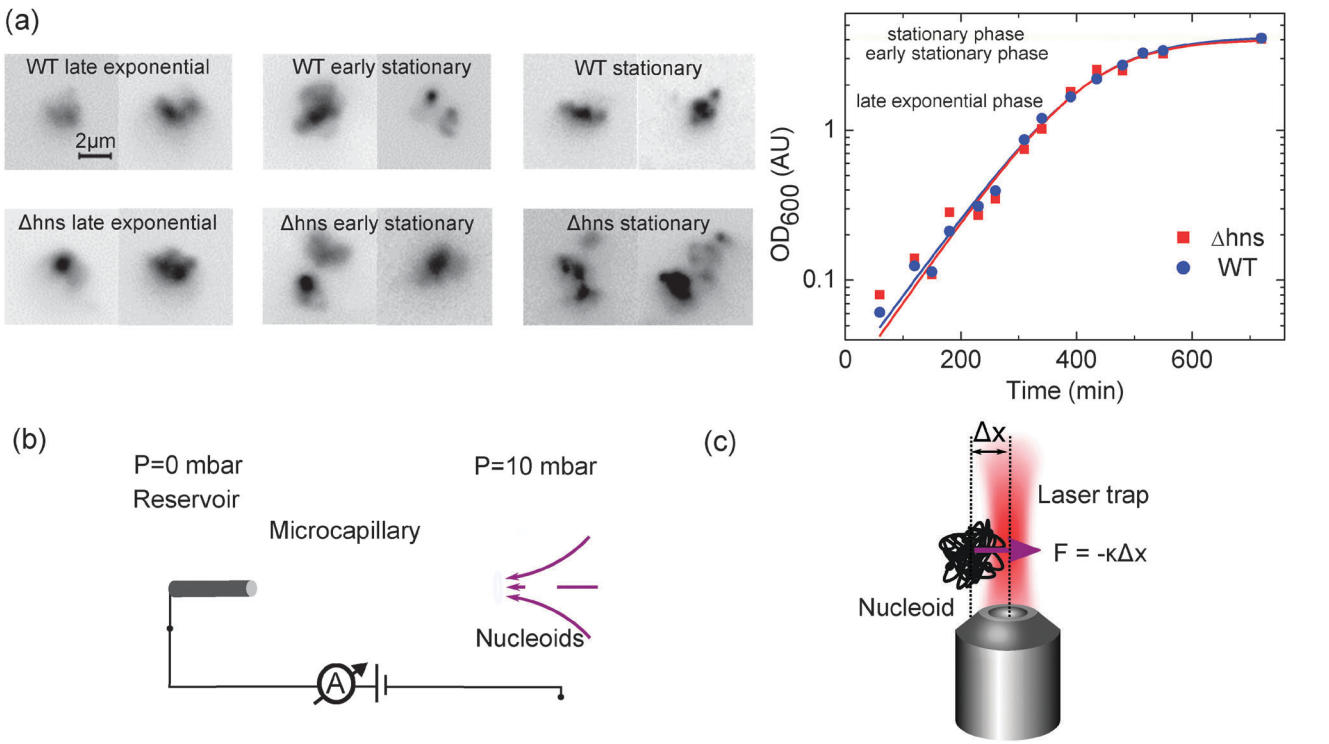


Fig. 1 An overview of the experimental techniques. (a) Representative fluorescence images of the nucleoids stained with DAPI (left) illustrate the large differences in the structure of WT and Δhns nucleoids qualitatively. Lightly stained areas correspond to lower DNA densities within the nucleoid. Nucleoids were obtained from the *E. coli* populations at the late exponential, early stationary and stationary growth phases as indicated on the growth curve (right). (b) Resistive pulse sensing of nucleoids: the reservoirs are filled with buffer and an excess pressure is applied to the reservoir on the right which drives the nucleoids through the microcapillary. (c) Drag measurements using optical tweezers: the laser trap is driven along a sinusoidal path with an amplitude of 3.1 μm. The force induced by the trap on the nucleoid (purple arrow) is proportional to the nucleoid displacement from the center of the trap and is balanced at all times by the hydrodynamic drag.

reservoir in front of the microcapillary. The nucleoid concentration is optimized to enable detection of the ionic current signature for between 500–800 single nucleoids over 20 minutes while avoiding aggregation of nucleoids in solution. The nucleoids are driven into the microcapillary by applying an excess pressure of 10 mbar.

A typical ionic current trace, containing the signals of many nucleoids translocating through the microcapillary, is shown in Fig. 2a. The single translocation events have a detailed characteristic "signature" as shown in the inset: the basic properties of this signature are the event duration and the maximum drop in ionic current (peak amplitude). Another important parameter is the total area of the translocation event, which, this being a plot of ionic current against time, gives an estimate of the charge excluded from the pore during the translocation.[35] We therefore expect that both the peak amplitude and the event area would increase with increasing nucleoid size. The baseline current in the microcapillary (the ionic current when there is no nucleoid in the pore) serves as a good indicator of microcapillary size.[32] To reduce the effect of the variation in diameter between different microcapillaries, we use data from microcapillaries with similar baseline currents (~30 nA at 500 mV). As a further measure, the amplitude, event duration and event area are normalized by dividing by the baseline current; these new parameters are termed "proportional amplitude", "proportional duration" and "proportional area" respectively.

### 2.2 Δhns nucleoids have distinct ionic current signatures by the early stationary phase

The results of the microcapillary measurements are presented in Fig. 2. Fig. 2b shows a scatter plot of proportional amplitude (on a logarithmic scale) against proportional duration for both WT and Δhns strains in late exponential and early stationary phases; each point corresponds to the translocation of a single nucleoid. In the late exponential phase, there is significant overlap in the scatter between the two strains. On the other hand, in the early stationary phase, the Δhns strain can be clearly distinguished from the WT strain indicating a population-wide change in nucleoid size. This trend is also evident in the proportional area histograms for the four data sets (Fig. 2b, right).

To further examine these trends we plot a normalized cumulative frequency count of the proportional amplitude for all data sets in Fig. 2c. The data in each scatter plot were fitted with a log-normal distribution with a peak value $\mu$ and width $\sigma$ as described in the Methods section. This analysis yields the mean value and standard deviation for each data set, shown in Fig. 4b. Each data set was also fitted with the superposition of two independent log-normal distributions, in order to account for the effect of partially replicated genomes.[39] A statistically significant second peak was only obtained for the WT population in the late exponential phase.

Both the Δhns and WT strains have a peak value at $\mu \approx 0.013$, whereas the WT population has an additional peak at $\mu \approx 0.004$. We believe this observation is consistent with the fact that the bacteria from which the nucleoids are extracted are dividing asynchronously while in the exponential phase, therefore at any instant in time bacteria at different stages in the replication cycle, and hence with varying amounts of DNA coexist.[39] The differences between the two strains are further amplified at the transition to stationary phase. The Δhns strain has a broad distribution with a peak at $\mu \approx 0.029$. On the other hand, the WT strain has a narrow distribution with a sharp peak at $\mu \approx 0.005$. These results point to two conclusions: (a) the Δhns strain has on average a larger purified nucleoid by the early stationary phase;

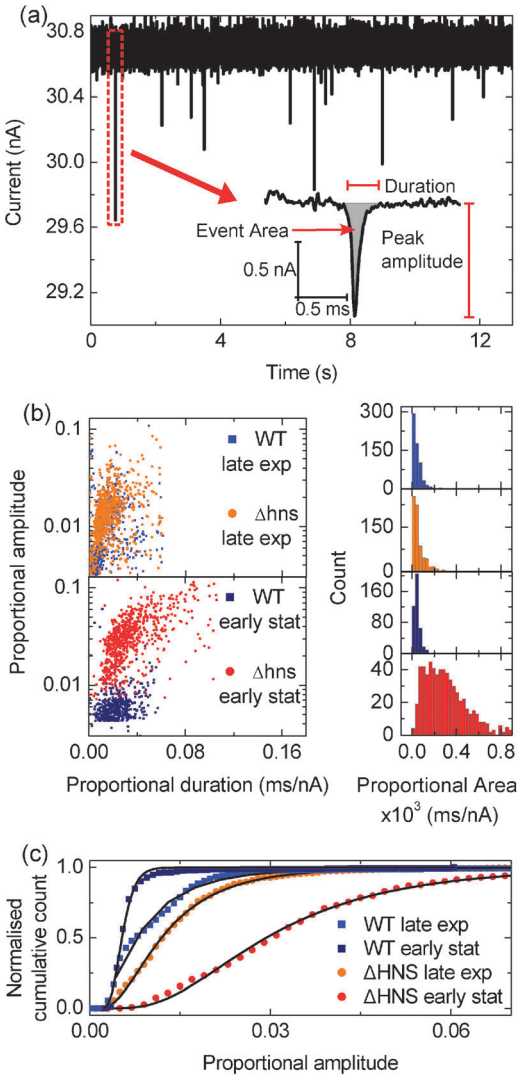


Fig. 2 Resistive pulse sensing in glass microcapillaries probes the physical state of nucleoids with high throughput (between 500 to 800 in each dataset) at the late exponential and early stationary phase. (a) An ionic current trace for a typical experiment showing many translocation events. One event is highlighted, and zoomed in the inset to illustrate the parameters that characterize the "signature" of each translocation event. (b) At late exponential phase, the scatter plot of proportional amplitude against proportional duration shows significant overlap between the two populations; in contrast at the early stationary phase the Δhns strain can be clearly distinguished from the WT strain. (c) The trend is further highlighted by the cumulative frequency plotted against the proportional amplitude for all datasets which is fitted with a log-normal distribution. The color scheme matches panels (a) and (b). By the early stationary phase, the proportional amplitude for Δhns is ≈6 times greater than for WT.

(b) the purified nucleoid in the WT strain appears to be compacted in the transition from the late exponential to the early stationary phase.

### 2.3 Overview of drag measurements with optical tweezers

Using optical tweezers, we measure the hydrodynamic radii of bacterial nucleoids. Optical tweezers[36,37] have often been used to perform active microrheology, in which a particle of known properties is dragged through a medium, and the rheology of the medium is extracted from the particle motion.[38] In the experiments here, this principle is turned around: the rheology of the aqueous medium is known, and hence the properties of the particle are measured. Nucleoids are trapped (Fig. 1c) and then driven along a sinusoidal path over a range of frequencies (see Fig. 3a). This allows us to probe the hydrodynamic drag experienced over this frequency range and to recover the drag coefficient. From this, we can obtain the hydrodynamic radius – a well-defined measure of the size of the nucleoids. The equation of motion for the nucleoids driven by the optical trap is that of an overdamped oscillator:

$$\kappa x + \xi \frac{\mathrm{d}x}{\mathrm{d}t} = \kappa L \exp(-i\omega t) \qquad (1)$$

where $\kappa$ is the stiffness of the trap, $x$ is the instantaneous position of the nuecloid, $\xi$ is the drag coefficient, $\omega$ is the trap driving frequency and $L$ is the amplitude of the laser driving force. Assuming a spherical shape of the nucleoid, the drag coefficient is given by the Stokes relationship for the drag on a spherical particle $\xi = 6\pi\eta R_{\mathrm{H}}$, where $\eta$ is the viscosity of the solution and $R_{\mathrm{H}}$ is the hydrodynamic radius of the particle.

The function $x = a\exp(-i(\omega t + \Delta\phi))$ is a solution to eqn (1). The displacement of the nucleoid thus has the same frequency $\omega$ but lags behind the trap potential by a phase difference $\Delta\phi$ and has a slightly reduced amplitude. The phases of the trap and nucleoid displacements are obtained from the arctangent of the complex amplitude at the peak value in the Fourier-transformed data, and if the phase difference $\Delta\phi$ is small then it is related to the physical parameters simply by:

$$\Delta\phi(\omega) = \frac{6\pi\eta}{\kappa} R_{\mathrm{H}}\omega \qquad (2)$$

*i.e.* it is a linear function of the angular frequency of the oscillations.

To accurately determine the phase shifts, it is crucial to record the positions of the trap simultaneously with the position of the nucleoid (extracted from image analysis), as shown in Fig. 3a. In the custom setup, the frame timings are synchronized with the laser beam position to within a microsecond, thus small phase shifts are clearly measurable within the precision of this technique. The trap stiffness ($\kappa$ = 3.9 pN μm$^{-1}$) was chosen to be soft enough in order to have large observable phase shifts, while allowing the nucleoid to be reliably trapped along the sinusoidal path for a wide range of frequencies. The inverse proportionality between $\kappa$ and $\Delta\phi(\omega)$ (eqn (2)) sets an upper limit on the angular frequency of the driven trap oscillations. To determine if the Stokes drag coefficient is constant, *i.e.* if the nucleoid is acting as a solid or a deformable body, it is important to perform experiments over a range of

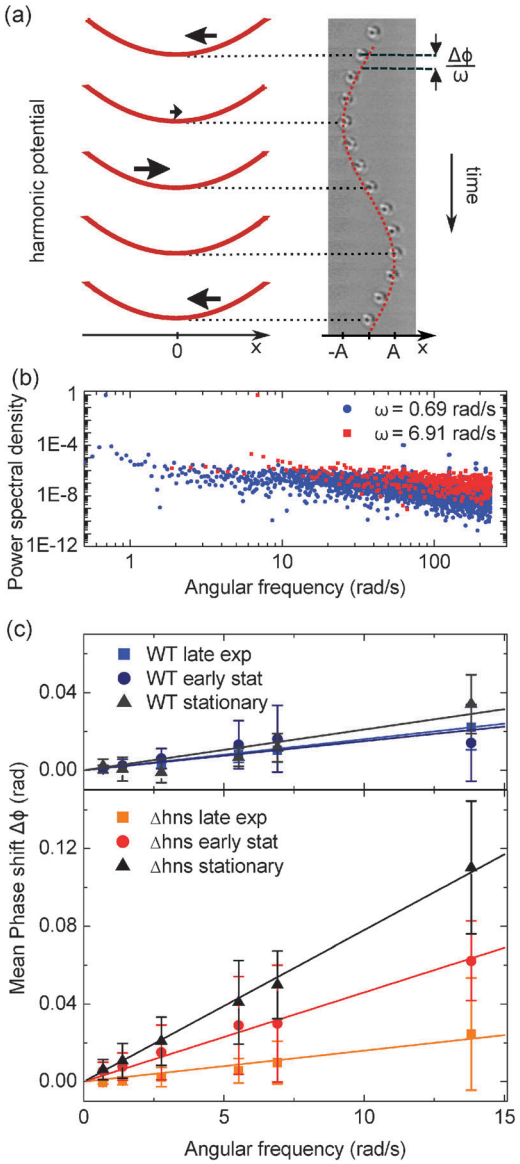


Fig. 3 The hydrodynamic radius of nucleoids can be measured directly with optical tweezers. (a) Individual nucleoids are subjected to a harmonic force (arrows) in the optical trap. The composite of selected frames recorded in the experiment shows the nucleoid advancing along a sinusoidal path, following that of the optical tweezers (red curve, shown with exaggerated phase shift $\Delta\phi$). Measurements of the positions of the nucleoid are synchronized with the trap positions, allowing $\Delta\phi$ to be obtained. (b) Power spectral density of the motion of a nucleoid at two driving frequencies as indicated in the legend. The peak in each spectrum corresponds exactly to the driving frequency. (c) Phase shifts are plotted as a function of the angular frequency for typically 5 nucleoids each from WT (upper panel) and Δhns (lower panel) strains at different stages of growth. Color scheme follows that of Fig. 2.

frequencies: 0.69, 1.38, 2.77, 5.53, 6.91 and 13.82 rad s$^{-1}$ were successful, while $\omega$ = 27.64 rad s$^{-1}$ resulted in incomplete sinusoidal cycles and is not presented here.

### 2.4 Δhns purified nucleoids expand when entering the stationary phase

Fig. 3b shows the power spectral density (PSD) of the motion of a nucleoid at $\omega$ = 0.69 and $\omega$ = 6.91 rad s$^{-1}$; the corresponding

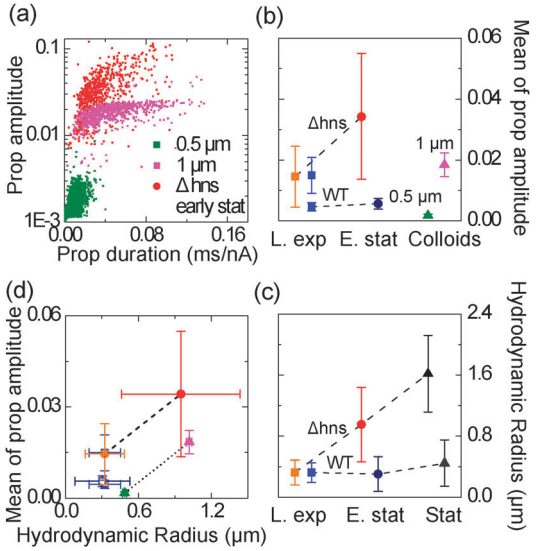


Fig. 4 Δhns nucleoids are larger than WT ones at early stationary phase and beyond. The comparison between translocation signals of solid particles and nucleoids indicates that they behave similarly in restricting the flow of ions. (a) The ionic current signatures for Δhns nucleoids in the early stationary phase are similar to those of 1 µm radius polystyrene colloids. The differences between both populations are revealed by the microcapillary (b) and tweezers (c) experiments. Both experiments confirm that Δhns nucleoids are larger than WT ones at late exponential phase and beyond (trends indicated by the dashed lines). The hydrodynamic radii obtained from the fitting in Fig. 3c are (late exp) WT: (0.32 ± 0.13) µm, Δhns: (0.32 ± 0.13) µm; (early stat) WT: (0.30 ± 0.22) µm, Δhns: (0.95 ± 0.48) µm; (stat) WT: (0.43 ± 0.3) µm, Δhns: (1.59 ± 0.51) µm respectively. (d) A plot of the mean value of proportional amplitude against the hydrodynamic radii for both strains of nucleoids in late exponential and early stationary phases as well as for the solid colloids. While there are no appreciable changes for the WT population (hollow markers), the Δhns nucleoids demonstrate a similar trend (dashed line) to the solid colloids (dotted line) with increasing hydrodynamic radius.

driving frequencies are clearly visible as peaks in the PSD. Fig. 3c shows the phase shift against driving frequency for nucleoids obtained at the different growth stages. We then obtain $R_H$ from a linear fit of $\Delta\phi(\omega)$ against $\omega$ from eqn (2). The hydrodynamic radii obtained by optical tweezers for nucleoids from different growth phases are summarized in Fig. 4c. There is no significant change (within the precision of this experiment) between the WT strain at different growth stages. In contrast, the size of the nucleoids from the Δhns strain appears to increase progressively as the bacteria leave exponential and enter stationary growth phase: the $R_H$ changes from 0.3 µm to 1.0 µm and 1.6 µm in the early stationary and stationary growth phase respectively. This shows that the nucleoid is expanding several fold above the volume that would be available in the cell, likely because of the release of osmotic compaction forces due to molecular crowding.[4,5,13] In later stages of growth we have observed nucleoids with protrusions (see Fig. 1a), which could account for the observed increase in $R_H$ in the samples obtained from bacteria lacking the H-NS protein. This is probably connected to different stages of ongoing replication and catenation of completely replicated genomes.[40]

### 2.5 Two complementary methods reveal that bacterial nucleoids are non-porous to flow

The resistive pulse technique enables us to compare bacterial nucleoids with solid polystyrene colloids of precisely known size. Fig. 4a shows a plot of proportional amplitude against proportional duration obtained for the translocation of 0.5 and 1 µm radii colloids and for the Δhns strain in the early stationary phase (hydrodynamic radius 1 µm). Although the shapes of the distributions are somewhat different, the considerable overlap indicates that the Δhns nucleoids behave similarly to the 1 µm radii colloids.

To support this further, we plot in Fig. 4d the mean value of the proportional amplitude for the populations studied with the resistive pulse technique (Fig. 4b) against the hydrodynamic radii obtained from the tweezers (Fig. 4c). The near parallel trendlines for both the Δhns nucleoids (dashed line) and colloids (dotted line) strongly suggest that the change in proportional amplitude scales with the hydrodynamic radius in the same manner for a solid colloid as it does for a nucleoid. The trend cannot be observed for the WT nucleoids as their size remains relatively constant. This demonstrates that for the purposes of ionic current measurements, the bacterial nucleoid, like a polystyrene colloid, can be considered as impermeable to the flow of ions.

## 3 Discussion

Let us first address the more technical, but relevant issue of the experiment calibration. In principle, it might be too simplistic to consider the nucleoids as solid objects: the driven motion by tweezers might lead to flow-induced deformation, changes in the drag coefficient, and hence to a frequency dependent $R_H$. Similarly, viscous shear in the microcapillary experiments could also deform the nucleoids, and in addition it is not *a priori* obvious that the nucleoid should behave as a solid rather than a porous object with regards to ionic flow permeability, making the interpretation of the ionic current signals not straightforward. Using data from Pelletier *et al.*,[4] we have estimated a bulk modulus of 30 kPa for nucleoids extracted in similar buffers. The translocation of the nucleoids into the microcapillary at velocities typical for the 10 mbar driving pressure used[41] can be estimated to produce a shear stress of 1 mPa. Our experiments should thus exert negligible strain on the nucleoids. Similarly, the absence of non-linear behavior at high driving frequencies in Fig. 3c indicates that the driven trap oscillations do not deform the nucleoids. We also directly compared the ionic current signatures of the nucleoids to polystyrene colloids. The parallel trendlines observed in Fig. 4d indicate that the nucleoids display a similar porosity to the flow of ions as the colloids. These results, when considered alongside a description of the nucleoid as a porous plug,[42] are consistent with a low surface charge density and dense packing of nucleoids. From all these observations, we can conclude that: (a) the nucleoids behave under these conditions as non-deformable solid colloids, impermeable to the flow of ions[41] and (b) post-calibration with colloids of known size, the proportional amplitude measured in the ionic current measurements provides a reliable estimate of the nucleoid size.

 

Resistive pulse sensing with microcapillaries is a continuous measurement technique that probes the properties of an individual nucleoid in under a millisecond in measurement buffers that can be varied easily. It can also be used for a study of the time-dependence of nucleoid properties. This distinguishes it clearly from other 'lab on a chip' measurement techniques.[4] In the present study, no systematic change in nucleoid properties was observed over the period of about 20 minutes.

The two techniques ideally complement each other to provide an overall picture of the changes in nucleoid structure at the single nucleoid level but on a population scale. Both experiments reveal that the purified Δhns nucleoid undergoes substantial expansion as the bacteria enter the late exponential phase. Our results also demonstrate that the H-NS protein present in the nucleoids extracted from WT bacteria entering the stationary phase reduces nucleoid expansion after lysis and release from the crowded cytoplasm. In the Δhns strain, this restraint on expansion is not present. This is likely due to the bridging action of H-NS, possibly also through the formation of foci such as those seen in Wang *et al.*[23] Our study can associate the onset of H-NS genome compaction activity to a specific growth-phase transition. It is also consistent with the recently observed expansion of H-NS occupancy regions upon entry into the stationary phase.[43,44] Note that this result might be unexpected, since H-NS is expressed at a fairly constant ratio with DNA along a growth curve.[45] As the growth rate slows down at the entry into the stationary phase, the compaction of the nucleoid by H-NS may be required to counter the loss of the compaction due to the activity of highly expressed ribosomal promoters in the exponential phase.[46] The 1.6 μm hydrodynamic radius measured for the Δhns strain entering the stationary phase is consistent with theoretical calculations for the expected size of supercoiled DNA released from a bacterium in the absence of proteins.[11,13]

In summary, we are able to, for the first time, study the physical properties of the nucleoid using high-throughput techniques. Our novel combination of techniques allows us to not only be able to size these structures but also study new properties such as the permeability of nucleoids to ionic flow. The application of such techniques immediately opens new avenues for bacterial chromosome research, such as probing the growth-phase dependent role of other relevant NAPs[47,48] in many single nucleoids as well as studying the physical properties of isolated nucleoids over extended time periods.

# 4 Materials and methods

## 4.1 Nucleoid preparation

The nucleoids were prepared from *E. coli* wild type MG1655 strain (WT) or from the same strain bearing a deletion in the gene encoding for the H-NS protein (Δhns).[43] The bacteria were cultured in liquid M9 media enriched with 0.4% Glucose and 0.5% Casamino acids at 37 °C. Previous studies with the Δhns strain grown in similar media[21] as well as nutrient rich LB media[22] at 37 °C have also obtained only a slight reduction in growth rates as compared to the WT strain. We used a low salt method[25] of osmotic shock to release the nucleoids from the cell – modified to include the cold shock step as described in ref. 13. The bacteria were harvested by centrifugation (5 min at 8000*g*, 4 °C) and immediately resuspended in ice cold sucrose buffer (20% sucrose w/v, 100 mM NaCl, 10 mM sodium phosphate buffer pH 7.4 and 10 mM EDTA). Lysosyme was added (200 μM final concentration) and the sample was removed from ice. It was incubated with lysozyme for 15–20 min and then osmotic shock was effected by diluting the buffer 100 fold. This is the nucleoid extraction buffer with a final concentration of 0.2% sucrose, 1 mM NaCl, 100 μM phosphate buffer, 100 μM EDTA and 2 μM lysosyme. Although recent evidence[13] suggests that even lower amounts of lysozyme allow the nucleoid to open further when extracted under low salt conditions, we use 2 μM lysosyme in the extraction buffer so as to ensure our data can be easily compared with previous experiments and data in the literature. The DAPI stain was added only for the acquisition of the illustrative fluorescence images shown in Fig. 1a. The nucleoids in the samples from late exponential and early stationary growth phases were reliably liberated using this method. By visual inspection and membrane staining, the occurence of 'ghosts' (nucleoids with attached cell wall debris) formed due to incorrect lysing was estimated to be under 10%. However in the stationary phase, even in the low salt buffer, up to 40% of lysozyme-treated bacteria did not release their DNA, forming spheroids instead.[25] This did not allow us to carry out the population-wide microcapillary experiments in a reliable manner, but still allowed us to perform the hydrodynamic drag experiments. The optical densities (ODs) measured at 600 nm at which the nucleoids were extracted are as follows: microcapillary experiments – WT: 1.80, 3.10; Δhns: 1.30, 3.07; optical tweezers experiments – WT: 1.39, 3.13, 4.10; Δhns: 1.36, 3.01, 4.04.

## 4.2 Microcapillary fabrication and passivation

Microcapillaries of between 3–10 μm diameter were fabricated from borosilicate glass capillaries (Hilgenberg GmbH) of outer diameter 0.5 mm and inner diameter 0.375 mm using a commercially available laser puller (P-2000, Sutter). Using an optical microscope, we were able to select microcapillaries of similar size and shape to each other. To prevent sticking of the bacterial nucleoids to the walls of the microcapillary, these were passivated with a layer of *N*-(triethoxysilylpropyl)-*O*-polyethylene oxide urethane. Briefly, the chemical was added to a 95 : 5 solution of EtOH in water at pH 2 to activate the silanol groups. The microcapillary was plasma activated and then dipped in this solution for a short period. The microcapillary was then heated to 110 °C (as part of the assembly into the PDMS mold) to enable the covalent attachment to the glass surface.

## 4.3 Pressure driven flow through microcapillaries

The coated microcapillaries were assembled into a custom designed PDMS chip.[49] Nucleoids were added to the reservoir containing the microcapillary and the two reservoirs were sealed using a perspex block. An excess pressure of 10 mbar was applied using a microfluidic flow control system (Fluigent, MFCS IV) to the reservoir containing the nucleoids. This produced

fast flows and further reduced the chances of blockage of the pore due to sticking to the walls. A bias voltage of 500 mV was maintained between the two reservoirs solely to enable the measurement of the ionic current through the pore. Ionic current through the microcapillary was detected using an amplifier (EPC 800, HEKA) and a DAQ card (PCIe-6351, National Instruments), acquired using LabVIEW and analyzed using Campfit. Individual events were analyzed using a threshold search with a noise rejection parameter value of 0.02 ms.

### 4.4 Optical trapping

The sample was prepared by depositing a 4 μL drop of final solution on a glass slide. A chamber was formed by placing a cover slip on a 150 μm thick double sided HybriWell adhesive spacer, precut to surround a circular sample space of diameter 8 mm. The nucleoid was held 60–80 μm above the glass surface in a potential trap created by custom built optical tweezers. The setup consists of a laser (CrystaLaser IRCL-2W-1064, 1064 nm, maximal power 2 W) focused through a water immersion objective (Nikon Plan Apo VC 60× WI 1.2 N.A.) mounted on a Nikon Eclipse Ti-E microscope. The laser beam was steered *via* a pair of Acousto Optical Deflectors (AODs) (AA Opto-Eectronic, AA.DTS.XY-250@1064 nm) controlled by custom built electronics, with sub-nanometre position resolution. The transmission of the AOD with respect to deflection angles was pre-adjusted so that the power level was uniform across all the trapping area. The maximal laser power at the trap was approximately 500 mW. The experiments were performed with a trap stiffness of 3.9 pN $\mu m^{-1}$, calibrated by measuring the width of the distribution of thermal displacements of the nucleoids in a stationary trap over approximately 5000 frames.[50] This trap stiffness corresponds to 20% of the laser's maximum power and creates a soft spring drive for the experiment. By driving solid colloidal particles, and examining the Lorentzian spectrum of fluctuations away from the drive frequency, it was also verified that the trap is harmonic up to the displacements that occur in the experiments. By collecting the CMOS camera frame times through the FPGA and microcontroller that also control the AOD laser deflection, the timing of each frame exposition can be synchronized to within a microsecond with the corresponding positions of the trap.

### 4.5 Hydrodynamic drag

The trap positions were assigned along a sinusoidal path of amplitude $A$ = 3.1 μm. The AOD update frequency is 20 kHz. The path was defined with 100 positions, and the beam switched through these at varying time intervals to generate the range of driving frequences. Images were acquired on a Marlin F-100B CMOS camera (Allied Vision Technologies) at 75.5 frames per s with an exposure time of 12 ms and each pixel corresponding to 0.11 μm. The nucleoid position was obtained using a correlation filter with a concentric kernel optimized to the profile of a nucleoid, followed by a 2D least-squares fit. This procedure gave the center of mass coordinates of the nucleoid with sub-pixel resolution.[50] The non-uniform shape of nucleoids was the biggest limiting factor in determining the center of mass accurately. The phase shift $\Delta\phi$ between the trajectory of the trap and the observed trajectory of the nucleoid was established from a Fourier transform of each section of data with fixed frequency.

### 4.6 Log-normal distribution curve fitting

The cumulative frequency plots shown in Fig. 2c are fitted with a log-normal distribution with a single peak. The cumulative distribution function of a log-normal distribution is given by:

$$\mathrm{CDF} = \frac{1}{2} + \frac{1}{2}\mathrm{erf}\left(\frac{\ln\ x - \mu}{\sqrt{2\sigma^2}}\right) \quad (3)$$

where $\mu$ is the peak value and $\sigma$ is the width. From these parameters the mean value ($E(X)$) and the standard deviation (SD) of the distribution are given by:

$$E(X) = \exp\left(\mu + \frac{\sigma^2}{2}\right) \quad (4)$$

$$\mathrm{SD} = \left(\exp\left(\sigma^2\right) - 1\right)^{\frac{1}{2}} \cdot E(X) \quad (5)$$

## Conflict of interest statement

None declared.

## Acknowledgements

We thank K. Dorfman, G. Fraser, I. Fishkov, O. Krichevsky, C. L. Woldringh and T. Odijk for useful comments and discussions and G. Fraser for the gift of the deletion mutant strain. This work was supported by the International Human Frontier Science Program Organization [RGY0069/2009-C to KB, BS, JK, MCL and PC]; Emmy Noether program [VVT, KB and UFK]; the Cambridge Commonwealth Trust [VVT]; and the Jawaharlal Nehru Memorial Trust [VVT].

## References

1 S. B. Zimmerman, *J. Struct. Biol.*, 2006, **156**, 255–261.
2 C. L. Woldringh and N. Nanninga, *J. Struct. Biol.*, 2006, **156**, 273–283.
3 N. Hadizadeh Yazdi, C. C. Guet, R. C. Johnson and J. F. Marko, *Mol. Microbiol.*, 2012, **86**, 1318–1333.
4 J. Pelletier, K. Halvorsen, B. Ha, R. Paparcone, S. Sandler, C. Woldringh, W. Wong and S. Jun, *PNAS*, 2012, **109**, E2649–2656.
5 T. Odijk, *Biophys. Chem.*, 1998, **73**, 23–29.
6 S. B. Zimmerman, *J. Struct. Biol.*, 2004, **147**, 146–158.
7 V. G. Benza, B. Bassetti, K. D. Dorfman, V. F. Scolari, K. Bromek, P. Cicuta and M. Cosentino Lagomarsino, *Rep. Prog. Phys.*, 2012, **75**, 076602–076624.
8 J. Wang and P. Levin, *Nat. Rev. Microbiol.*, 2009, **7**, 822–827.
9 C. J. Dorman, *Nat. Rev. Microbiol.*, 2013, **11**, 349–355.
10 D. Browning, D. Grainger and S. Busby, *Curr. Opin. Microbiol.*, 2010, **13**, 773–780.
11 T. Odijk, *Phys. A.*, 2000, **277**, 62–70.

 

12 S. Cunha, T. Odijk, E. Suleymanoglu and C. L. Woldringh, *Biochimie*, 2001, **83**, 149–154.
13 A. S. Wegner, S. Alexeeva, T. Odijk and C. L. Woldringh, *J. Struct. Biol.*, 2012, **178**, 260–269.
14 S. Rimsky and A. Travers, *Curr. Opin. Microbiol.*, 2011, **14**, 136–141.
15 F. C. Fang and S. Rimsky, *Curr. Opin. Microbiol.*, 2008, **11**, 113–120.
16 R. Amit, A. B. Oppenheim and J. Stavans, *Biophys. J.*, 2003, **84**, 2467–2473.
17 R. Dame, M. Noom and G. Wuite, *Nature*, 2006, **444**, 387–390.
18 P. Wiggins, R. Dame, M. Noom and G. Wuite, *Biophys. J.*, 2009, **97**, 1997–2003.
19 C. Lim, S. Lee, L. Kenney and J. Yan, *Sci. Rep.*, 2012, **2**, 509.
20 E. Bouffartigues, M. Buckle, C. Badaut, A. Travers and S. Rimsky, *Nat. Struct. Mol. Biol.*, 2007, **14**, 441–448.
21 T. Atlung and F. G. Hansen, *J. Bacteriol.*, 2002, **184**, 1843–1850.
22 R. Srinivasan, D. Chandraprakash, R. Krishnamurthi, P. Singh, V. F. Scolari, S. Krishna and A. S. N. Seshasayee, *Mol. BioSyst.*, 2013, **9**, 2021–2033.
23 W. Wang, G.-W. Li, C. Chen, X. S. Xie and X. Zhuang, *Science*, 2011, **333**, 1445–1449.
24 S. Maurer, J. Fritz and G. Muskhelishvili, *J. Mol. Biol.*, 2009, **387**, 1261–1276.
25 S. Cunha, C. L. Woldringh and T. Odijk, *J. Struct. Biol.*, 2005, **150**, 226–232.
26 T. Romantsov, I. Fishov and O. Krichevsky, *Biophys. J.*, 2007, **92**, 2875–2884.
27 S. Cunha, C. Woldringh and T. Odijk, *J. Struct. Biol.*, 2001, **136**, 53–66.
28 C. Murade, V. Subramaniam, C. Otto and M. Bennink, *Biophys. J.*, 2009, **97**, 835–843.
29 W. Coulter, *Proc. Natl. Electron. Conf.*, 1956, **12**, 1034–1042.
30 H. E. Kubitschek, *Nature*, 1958, **182**, 234–235.
31 J. J. Kasianowicz, *PNAS*, 1996, **93**, 13770–13773.
32 L. J. Steinbock, G. Stober and U. F. Keyser, *Biosens. Bioelectron.*, 2009, **24**, 2423–2427.
33 V. V. Thacker, S. Ghosal, S. Hernández-Ainsa, N. A. W. Bell and U. F. Keyser, *Appl. Phys. Lett.*, 2012, **101**, 223704.
34 N. A. W. Bell, V. V. Thacker, S. M. Hernandez-Ainsa, M. E. Fuentes-Perez, F. Moreno-Herrero, T. Liedl and U. Keyser, *Lab Chip*, 2013, **13**, 1859–1862.
35 J. Li, M. Gershow, D. Stein, E. Brandin and J. A. Golovchenko, *Nat. Mater.*, 2003, **2**, 611–615.
36 A. Ashkin, J. Dziedzic and T. Yamane, *Nature*, 1987, **330**, 769–771.
37 D. Grier, *Nature*, 2003, **424**, 810–816.
38 P. Cicuta and A. M. Donald, *Soft Matter*, 2007, **3**, 1449–1455.
39 C. Stokke, I. Flåtten and K. Skarstad, *PLoS One*, 2012, **7**(2), e30981.
40 O. Espeli, C. Levine, H. Hassing and K. Marians, *Mol. Cell*, 2003, **11**, 189–201.
41 G. Stober, L. J. Steinbock and U. F. Keyser, *J. Appl. Phys.*, 2009, **105**, 084702–084708.
42 R. O'Brien and W. Perrins, *J. Colloid Interface Sci.*, 1984, **99**, 20–31.
43 C. Kahramanoglou, A. S. N. Seshasayee, A. I. Prieto, D. Ibberson, S. Schmidt, J. Zimmermann, V. Benes, G. M. Fraser and N. M. Luscombe, *Nucleic Acids Res.*, 2010, **39**, 2073–2091.
44 M. Zarei, B. Sclavi and M. Cosentino Lagomarsino, *Mol. BioSyst.*, 2013, **9**, 758–767.
45 S. C. Dillon and C. J. Dorman, *Nat. Rev. Microbiol.*, 2010, **8**, 185–195.
46 J. E. Cabrera, C. Cagliero, S. Quan, C. L. Squires and D. J. Jin, *J. Bacteriol.*, 2009, **191**, 4180–4185.
47 P. Dupaigne, N. K. Tonthat, O. Espéli, T. Whitfill, F. Boccard and M. A. Schumacher, *Mol. Cell*, 2012, **48**, 560–571.
48 H. Niki, A. Jaffé, R. Imamura, T. Ogura and S. Hiraga, *EMBO J.*, 1991, **10**, 183–193.
49 L. J. Steinbock, O. Otto, C. Chimerel, J. Gornall and U. F. Keyser, *Nano Lett.*, 2010, **10**, 2493–2497.
50 M. Leoni, J. Kotar, B. Bassetti, P. Cicuta and M. Cosentino Lagomarsino, *Soft Matter*, 2009, **5**, 472–476.